Physical Dosimetry and Spectral Characterization of Neutron Sources for Neutron Capture Therapy

13

David W. Nigg

Contents

13.1 Introduction 228

13.2 Neutron Activation Spectrometry 229
13.2.1 Physical and Mathematical Basis 230
13.2.2 Practical Application 236

13.3 Gas-Filled Detectors 242
13.3.1 Ion Chambers 242
13.3.2 BF_3 and ^3He Detectors 245
13.3.3 Proton-Recoil Spectrometers 246
13.3.4 Fission Chambers 247

13.4 Additional Techniques 248
13.4.1 Scintillators 248
13.4.2 Thermoluminescent Dosimeters 249
13.4.3 Gel Detectors 250
13.4.4 Superheated Nucleation Detectors 250
13.4.5 Semiconductor Detectors 252
13.4.6 Self-Powered Neutron Detectors 253

References 254

D.W. Nigg
Nuclear Science and Engineering Division, Idaho National Laboratory,
MS 3860, P.O. Box 1625, Idaho Falls, ID 83415-3860, USA
e-mail: david.nigg@inl.gov

W.A.G. Sauerwein et al. (eds.), *Neutron Capture Therapy*,
DOI 10.1007/978-3-642-31334-9_13,

13.1 Introduction

In this chapter, we consider the experimental macroscopic physical dosimetry of neutron beams useful for boron neutron capture therapy (BNCT). Such neutron beams may be produced by small nuclear reactors or by particle accelerators and may be of the following types, categorized by their dominant ranges of neutron energy (E_n):

- Thermal beams ($E_n < 0.414$ eV) for cell and small-animal research.
- Hyperthermal ($E_n \sim 1$ eV) and epithermal ($0.414\ \text{eV} < E_n < 10$ keV) beams for small- and large-animal research and for human clinical applications.
- Fast-neutron ($E_n > 10$ MeV) beams for NCT-augmented fast-neutron therapy (NCT-FNT).

With minor variations, the techniques of macroscopic dosimetry covered in this chapter are applicable to all four beam types listed above. A detailed quantification of the spectral quality and physical dosimetric characteristics of the neutron source to be used is a key prerequisite for the practical application of BNCT. These characteristics include the following:

- The free-field neutron flux spectrum and intensity.
- Neutron-induced dose rates in standard phantoms and tissue resulting from neutron interactions that produce high linear energy transfer (LET) charged particles. Such particles include recoil protons from elastic scattering by hydrogen, 600 keV protons resulting from thermal neutron capture in nitrogen, and of course the alpha particles and lithium ions produced by neutron capture in boron, where boron is present.
- The dose rate of the incident photon component in the beam as well as the induced photon dose component, largely due to capture of thermal neutrons by hydrogen in tissue.
- Additional minor dose components due to neutron interactions with other tissue constituents, for example, neutron capture by chlorine and, at high energies, heaver ions resulting from elastic scatter by elements other than hydrogen. The latter interactions are ordinarily of significance only for NCT-FNT.

This information is required for confirmation that the neutron beam is in fact performing as intended, for use as input data in detailed radiation transport models of the patient anatomy used in treatment planning and clinical dosimetry, and for use as an aid in interpreting the results of preclinical and clinical studies. In recognition of this, the international BNCT research community has made significant efforts to identify and standardize certain key techniques and protocols that have been found useful. It is the intent of this article to offer a summary description of these, along with key supporting references, as a starting point and guide to further study for the practitioner entering this field of radiation oncology.

The scope of the discussion will be focused on the experimental quantification of the macroscopic *physical* performance characteristics of neutron beams for BNCT and their small, but inevitable, photon components incident to the neutron source production and the spectral tailoring process. Brief descriptions of advanced

radiation transport computational techniques and models useful as aids for experiment planning and beam performance data interpretation are also included.

The discussion is organized according to the various radiation measurement techniques that are commonly employed for physical dosimetry. It is assumed that the reader has some background and experience with radiation measurements at roughly the level of the classic texts by Knoll [33] and Attix [6]. A relatively detailed description of neutron activation spectrometry, generally viewed as the most robust (and the most reproducible and accurate) approach to the determination of the intensity and energy dependence of neutron sources used for BNCT will be presented first. Applications of gas-filled radiation detectors, both to provide additional neutron information and to separately quantify the incident photon component of the neutron source and the induced photon component in tissue, will then be covered. Finally, some specialized techniques that are useful in many situations are briefly summarized. Some recommended additional survey references for many of these subjects include Harker et al. [26], Rogus et al. [53], Järvinen and Voorbraak [31], Munck af Rosenschöld et al. [41], Auterinen et al. [7], Blaumann et al. [12], and Moss et al. [40].

It is important to note that the closely related field of treatment planning for BNCT is covered in a separate chapter. Discussions are also provided elsewhere for microdosimetry, the study of the basic physical and chemical mechanisms of radiation dose delivery on the cellular and subcellular levels of spatial resolution [55, 60, 61, 65]. This is also the case for biological dosimetry, the in vitro and in vivo study of the observable radiobiological effects that are induced in living organisms by neutron beams acting alone and in conjunction with the BNCT process [17, 46, 64]). The latter two fields are of crucial importance for the understanding of the biological effects of a given neutron beam (and of the BNCT process itself) and are dependent in turn on the physical characteristics of the neutron beam of interest, as is the treatment planning process.

Finally, it is important to recognize the importance of accurate and reproducible physical beam dosimetry as an essential tool for combination and intercomparisons of preclinical and clinical results from different centers. To this end, an international BNCT dosimetry exchange was conducted recently by the clinical BNCT research centers in Europe and in the Americas. This exchange has also served as a mechanism for further refinement and standardization of the most widely used experimental methods described here. Further details of this important effort are provided by Binns et al. [10, 11] and Riley et al. [50, 51].

13.2 Neutron Activation Spectrometry

Neutron activation spectrometry is based on the fact that different elements (and different isotopes of the same element) placed in a neutron beam will capture and scatter neutrons selectively with respect to the incident neutron energy. Some elements are primarily sensitive to capture of thermal neutrons; others have strong capture resonances in the epithermal energy range, while others exhibit interaction

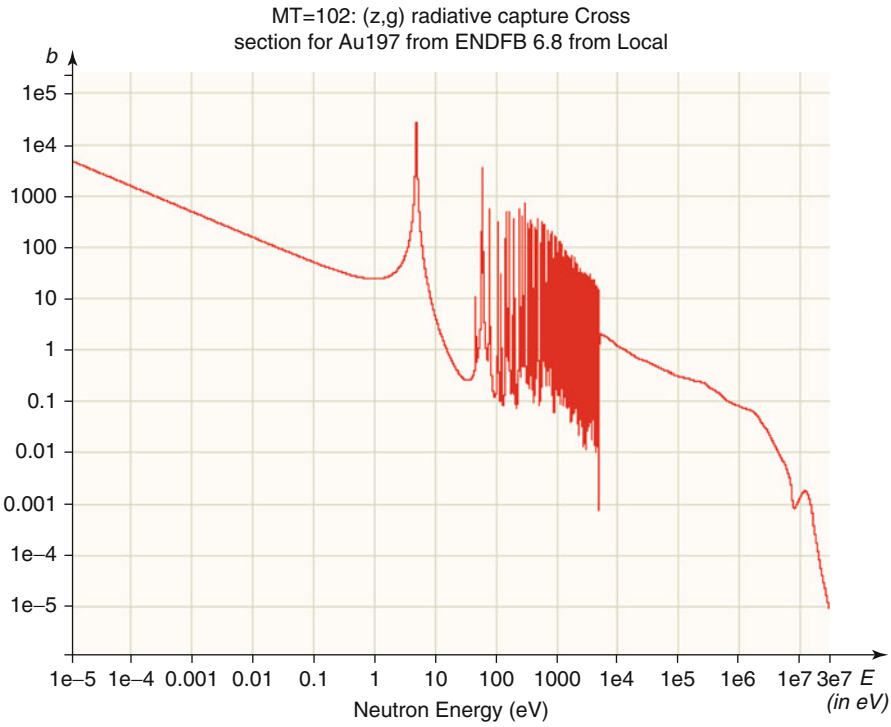

Fig. 13.1 Capture cross section (barns) of ^{198}Au (*Source*: OECD Janis 2.1)

energy thresholds for inelastic scatter, secondary neutron and charged particle emission, and fission, below which essentially no interactions occur. If the neutron interaction product for a particular nuclide is radioactive, then the induced radioactivity of a sample of that nuclide placed in a neutron beam will be largely proportional to the neutron flux at energies where interactions are most likely to occur in the sample. If different materials having different sensitivities to neutrons as functions of energy are activated in the same beam, it is ultimately possible to reconstruct a measured neutron spectrum from the induced activities. The level of spectral detail that can be reliably obtained generally corresponds to the number of different materials, and different interactions in the same materials, that are available.

13.2.1 Physical and Mathematical Basis

As an example to illustrate the underlying physics of activation spectrometry, Fig. 13.1 shows the capture cross section for ^{197}Au, which has a relatively high thermal neutron capture component as well as a prominent capture resonance at about 5 electron volts (eV). Capture of neutrons in a small sample (typically a foil or wire) of ^{197}Au produces ^{198}Au, which undergoes beta decay with emission of a

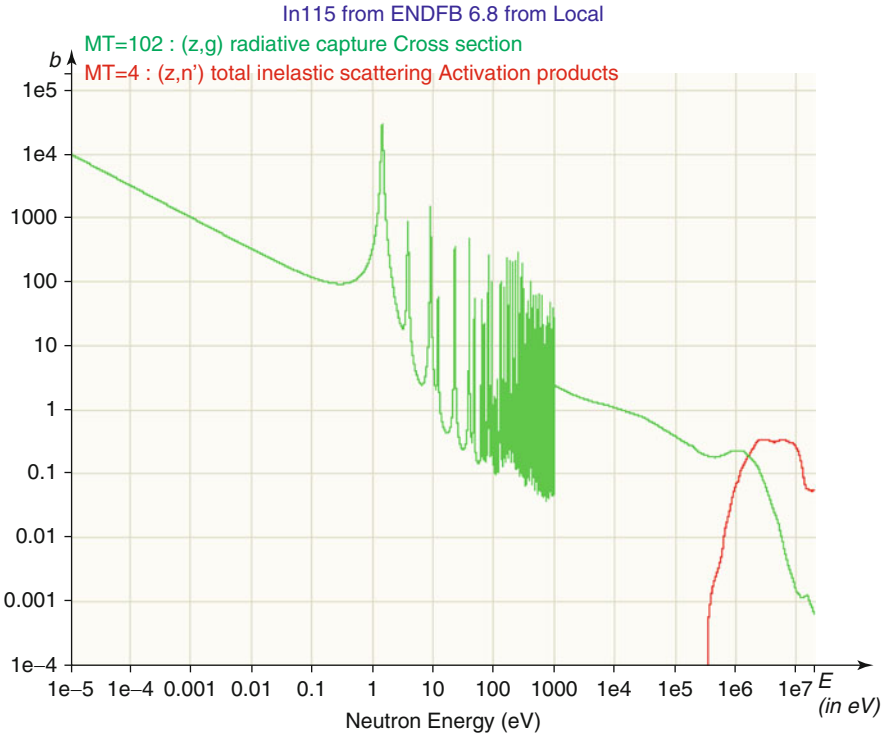

Fig. 13.2 Capture (*green*) and inelastic scatter (*red*) cross sections (barns) of ^{115}In (*Source*: OECD Janis 2.1)

prominent 0.411 keV gamma ray. The strength of this gamma ray is proportional to the neutron capture rate, which is for the most part proportional to the flux of neutrons at thermal energies and at 5 eV. If the sample is placed inside a cover made of cadmium, which absorbs essentially all incident thermal neutrons, then the interaction rate of the gold sample will be proportional to the neutron flux above thermal energies, primarily at 5 eV where the resonance occurs. The thermal and above-thermal neutron fluxes can then be separated by converting the measured induced activities to saturation activities (i.e., activation rates per atom), subtracting the activation rate of the cadmium-covered sample from that of the bare sample and computing the corresponding thermal neutron and total neutron fluxes. This is the classic cadmium difference method, and in effect it yields a two-energy group (thermal and above-thermal) spectrum. Elemental gold also exhibits several very useful and convenient threshold interactions for secondary neutron emission. These include (n,2n) up through (n,6n), covering the entire neutron energy range of interest for NCT as well as FNT, extending up to about 60 MeV [43].

As another example, cross-section data for ^{115}In are shown in Fig. 13.2. This nuclide (96 % abundance in natural indium) captures thermal neutrons, and it also has a strong neutron capture resonance at about 1 eV. In both cases, neutron capture

produces radioactive ^{116}In, which emits three prominent gamma rays with energies of 416, 1,097, and 1,293 keV. In addition, it will form an isomer by inelastic scatter of neutrons above about 400 keV. This yields ^{115m}In, which decays back to the ground state by emission of a 336 keV gamma ray. Hence, the inelastic scatter rate (and thus the neutron flux above the 400 keV threshold) is proportional to the measured activity of the 336 keV gamma ray, while the activities of the other three gamma rays, which also incidentally have a different half-life since they are associated with a different radionuclide (^{116}In), are largely proportional to the neutron flux at thermal energies and at 1 eV. If an indium foil is covered with cadmium, the thermal neutron capture rate is suppressed as described previously for gold. As a result, this single nuclide can be used to obtain information in three different energy ranges of the neutron spectrum of interest.

In the general case, a number of different activation responses (typically 8–12) are typically measured using a variety of different nuclides having different sensitivities to neutrons in the thermal, resonance, and fast-energy ranges. This permits the reconstruction of additional spectral detail in the unfolding process. Materials found useful for BNCT applications include gold and indium as described above, as well as copper, manganese, cobalt, dysprosium, uranium, copper, scandium, nickel, aluminum, and lanthanum.

We now consider some essential mathematical details of neutron activation spectrometry. In general, the volume-average activation rate per atom for a foil or wire dosimeter placed in a neutron flux field may be calculated as:

$$R = \int_0^\infty \sigma_d(E)\Psi_d(E)\mathrm{d}E \tag{13.1}$$

where $\sigma_d(E)$ is the microscopic activation cross section of interest for the dosimeter material, as a function of neutron energy, and $\psi_d(E)$ is the volume-average scalar neutron flux existing within the active dosimeter, again as a function of energy, and accounting for self-shielding effects, if any. Equation 13.1 can also be expressed as:

$$R = \int_0^\infty \sigma_d(E)\left(\frac{\Psi_d(E)}{\Psi(E)}\right)\Psi(E)\mathrm{d}E = \int_0^\infty \sigma_d(E)P_d(E)\Psi(E)\mathrm{d}E \tag{13.2}$$

where $\psi(E)$ is the unperturbed neutron flux that would exist at the measurement location in the absence of the flux perturbations caused by the dosimeter itself and any surrounding spectral modification devices and other structures placed in the beam (Cd covers, foil and wire positioning devices, etc.).

It may be noted here that, as a practical matter, the function $P_d(E)$ in Eq. 13.2 can be determined independently from $\Psi(E)$ if desired since it is simply a flux ratio. In this case, $\Psi(E)$ on the far right-hand side of Eq. 13.2 can be any appropriate a priori free-beam unperturbed flux estimate that is then modified by the self-shielding function $P_d(E)$.

Equation 13.2 may be written as a summation rather than as an integral by partitioning the range of the energy variable into a number of discrete contiguous energy groups:

$$R = \sum_{j=1}^{\mathrm{NG}} a_j \phi_j \tag{13.3}$$

where NG is the total number of energy groups,

$$a_j = \frac{\int_{\mathrm{EL}_j}^{\mathrm{EH}_j} \sigma_{\mathrm{d}}(E) P_{\mathrm{d}}(E) \Psi(E) \mathrm{d}E}{\int_{\mathrm{EL}_j}^{\mathrm{EH}_j} \Psi(E) \mathrm{d}E} \tag{13.4}$$

and

$$\phi_j = \int_{\mathrm{EL}_j}^{\mathrm{EH}_j} \Psi(E) \mathrm{d}E. \tag{13.5}$$

where EL_j and EH_j are the lower and upper energy limits of energy group j.

If additional dosimeter materials are placed in the beam, or if a particular material exhibits more than one independent activation response (e.g., gold or indium as noted earlier), then Eq. 13.3 may be written as a system of equations:

$$R_i = \sum_{j=1}^{\mathrm{NG}} a_{ij} \phi_j \tag{13.6}$$

where R_i is the total activation rate for interaction i and a_{ij} is the activation constant from Eq. 13.4 for reaction i due to neutrons in energy group j. There will be a total of NF equations, where NF is the total number of activation responses available.

Effective shielded cross sections $\sigma_{\mathrm{d}}(E)$ and the corresponding shielded and unshielded a priori neutron fluxes suitable for computing the function $P_{\mathrm{d}}(E)$ in the above equations may be obtained by any of several well-established neutron transport modeling techniques and nuclear data libraries. A typical approach involves computation of application-specific cross sections and a priori fluxes for each dosimeter in the beam using Monte Carlo techniques, for example, MCNP [14]. This is crucial if self-shielding or mutual shielding (as in a stack of foils) is significant. The Monte Carlo calculations for dosimeter packages generally include only the dosimeters and surrounding support structure with a representation for the incoming space-, angle-, and energy-dependent incident neutron source that has been precomputed using a Monte Carlo or deterministic computational model of the entire neutron beamline upstream from the irradiation location. The beamline computations may also be done with MCNP, or with a standard multidimensional discrete-ordinates

code such as DORT [49, 63]. It is also possible to use highly dilute foils [7] to avoid the need for a self-shielding correction, facilitating the direct application of standard dosimetry cross-section libraries. The dosimeter packages can usually also be designed to avoid mutual shielding, depending on the desired application.

The system of activation equations, Eq. 13.6, may be written out in matrix form as:

$$\begin{bmatrix} a_{11} & a_{12} & a_{12} & \cdots & a_{1\mathrm{NG}} \\ a_{21} & a_{22} & a_{23} & \cdots & a_{2\mathrm{NG}} \\ a_{31} & a_{32} & a_{33} & \cdots & a_{3\mathrm{NG}} \\ \vdots & \vdots & \vdots & & \vdots \\ \vdots & \vdots & \vdots & & \vdots \\ a_{\mathrm{NF1}} & a_{\mathrm{NF2}} & a_{\mathrm{NF3}} & & a_{\mathrm{NF\,NG}} \end{bmatrix} \begin{bmatrix} \phi_1 \\ \phi_2 \\ \phi_3 \\ \vdots \\ \phi_{\mathrm{NG}} \end{bmatrix} = \begin{bmatrix} R_1 \\ R_2 \\ R_3 \\ \vdots \\ \vdots \\ R_{\mathrm{NF}} \end{bmatrix} \tag{13.7}$$

or, more compactly:

$$[A][\Phi] = [R] \tag{13.8}$$

Equation 13.7 is exact, provided that the reaction rates R_i, the activation constants a_{ij}, and the group fluxes φ_j, are all self-consistent. If experimentally *measured* reaction rates (as opposed to the a priori reaction rates) for each interaction R_i are substituted into Eq. 13.7, a solution of the resulting new system of equations for "measured" fluxes corresponding to the measured reaction rates may also be obtained under certain conditions.

If NF = NG in Eq. 13.7, then the matrix [A] is square, its inverse will ordinarily exist, and the unknown flux vector may be obtained by any standard solution method that converges, provided that the rows of [A] are linearly independent to a sufficient degree and the measured reaction rates are sufficiently precise. In physical terms, the former requirement implies that the response functions (cross sections) for the activation interactions used in the measurement must be selected such that they have sufficiently different shapes as functions of energy. Spectral modification devices (e.g., cadmium covers) can also be used to force linear independence. It may be noted that positive fluxes are not guaranteed to result from this procedure, but if the elements of [A] are computed in a sufficiently valid, physically realistic manner for the specific measurement configuration and if the measured reaction rates are accurately determined, a positive solution will generally be obtained. In practice, this situation (NF = NG) is exemplified by the previously noted cadmium difference method, which can readily be shown to be a special case of Eq. 13.7, with only two rows in the matrix, one for the bare foil and one for the covered foil. It also typically occurs when measuring pointwise fluxes at resonance energies [26] using stacks of foils and when measuring simple spectra in phantoms using flux wires composed of alloys of two materials with different spectral responses, such as copper and gold, or manganese and gold.

There are two possibilities for the situation where NF, the number of available activation response functions, is not equal to NG, the number of energy groups for which it is desired to obtain unfolded fluxes. If NF < NG, the problem is underdetermined and additional information must be introduced in some manner to permit a solution, as is done in the various types of "adjustment" techniques for spectrum estimation from activation data. These methods involve the numerical modification of an input a priori spectrum to produce calculated responses that give the best overall match to the measured responses in a least-squares sense. If NF > NG, the problem is overdetermined and the "extra" information that is thereby available can be incorporated into the determination of a unique solution for the group fluxes and their propagated uncertainties by a linear least-squares procedure [43]. This "direct" unfolding method has an advantage in that it converges to a single unique solution.

The "adjustment" methods for spectral unfolding allow the estimation of a spectrum having more energy detail than the number of linearly independent activation responses, but with one exception, these do not produce a unique solution – many solutions are possible from the same input data. A unique solution can be obtained only by the generalized least-squares method, which requires covariance information for all of the input parameters, including the input spectrum as well as the activation cross sections and the measured responses. This covariance information in effect constrains the solution to a single physically realistic optimum in a least-squares sense. Several adjustment codes based on this approach have been developed. A popular example is the LSL code [57].

If the covariance information required for least-squares adjustment procedures is not available, other somewhat more empirical adjustment techniques are widely used, one popular example being the method described by Draper [20], implemented as an option in the SAND-II code [38]. Effective use of such methods requires good physical insight and intuition, as the form of the input a priori spectrum and its assumed uncertainty, as well as the iteration strategy used to produce a solution, can have a significant influence on the results. A more complete review of the various spectral unfolding and adjustment methods is provided by Järvinen and Voorbraak [31] or in any of several other comprehensive sources widely available in the neutron physics literature.

Neutron activation spectrometry can be applied to any neutron field for which suitable activation responses can be measured, either in air, in a phantom, or in vivo. It is used worldwide as a primary recommended method for characterization of epithermal neutron beams [10, 11, 31]. It has also been successfully applied to thermal neutron beams (e.g., [15]) and to accelerator-driven fast-neutron beams intended for use in BNCT-augmented fast-neutron therapy (e.g., [43]). It is capable of high precision (<5 %) if experimental uncertainties are carefully managed throughout every step of the process. Precautions to be taken include the following:

- Use of high-purity, accurately assayed activation materials
- Careful weighing, preparation, and handling of the foil packages to ensure accurate knowledge of the foil masses and to avoid contaminants
- Careful recording of the activation and post-irradiation decay times of the foils
- Irradiation at constant flux if at all possible

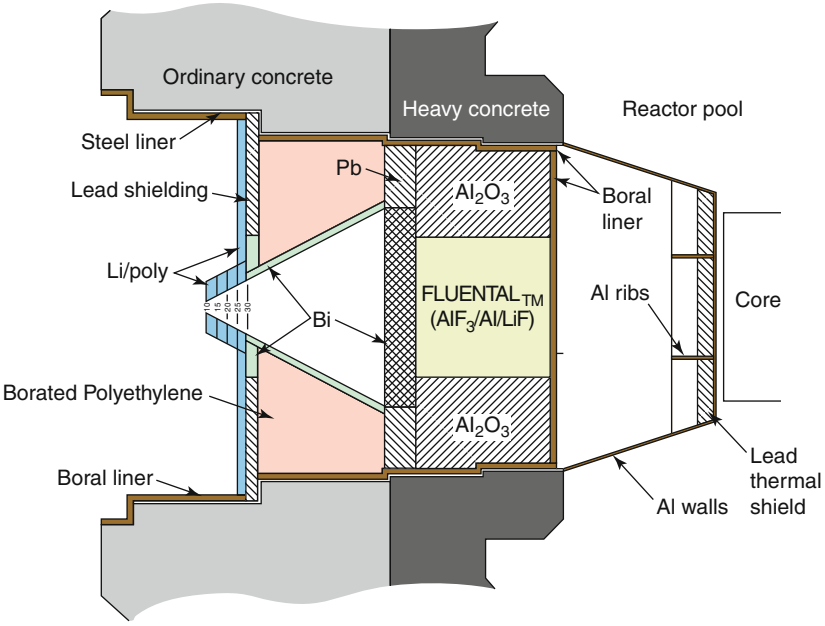

Fig. 13.3 WSU epithermal neutron beamline components. The reactor core is on the right

- Accurate, reproducible calibration of gamma spectrometers used for measurement of the foil activities, using certified, traceable standards
- Use of good techniques for the foil activity measurements in order to minimize uncertainties due to coincidence summing, counting geometry, etc.
- Thoughtful selection and application of unfolding techniques
- Use of multiple unfolding techniques to verify consistency

It is also important to recognize that in vivo activation measurements, especially in the case of thermal neutron beams, must be interpreted very carefully due to large flux gradients that depend on the specific target geometry, which can change in time and from one animal to the next because of respiration, motion, and other effects. As a result, reproducibility can be an issue and direct comparison with corresponding phantom measurements can be problematic.

13.2.2 Practical Application

Some recent measurements performed for the epithermal neutron beam constructed for preclinical BNCT research at Washington State University [44] provide a basic but illustrative example of an application of activation spectrometry for BNCT. Figure 13.3 shows a schematic diagram of the WSU epithermal neutron beam facility. The 1 MW WSU TRIGA™ reactor core is suspended from a movable bridge spanning an open pool. It can be positioned directly adjacent to a truncated

Fig. 13.4 Beam collimator installation at WSU showing the collimator with square exit port collar and lower borated polyethylene shielding

aluminum cone that extends horizontally into the reactor pool from the tank wall. This cone and the adjacent thermal column region penetrating the reactor shield monolith were originally filled with graphite. The epithermal neutron beam extraction components are located in this region.

A key distinguishing feature of the WSU facility is the incorporation of the high-efficiency neutron moderating and filtering material Fluenthal™, developed by the Technical Research Centre of Finland, into the design. A block of this material, which is composed of aluminum, aluminum fluoride, and lithium fluoride, is surrounded by aluminum oxide to produce the neutron filtering and moderating region shown in the figure. MCNP [14] and DORT [49] radiation transport design calculations using the BUGLE [54] cross-section library indicated that a free-beam epithermal neutron flux of approximately 10^9 n/cm^2-s would be produced at the irradiation position with the reactor core optimally loaded and operated at the design power of 1 MW. The background neutron kerma rate per unit useful epithermal neutron flux (a measure of the fast-neutron contamination) for the beam was calculated to be approximately 3.0×10^{-11} cGy/n-cm^2.

Figure 13.4 shows the bismuth collimator installation. The downstream end of the collimator is fitted with a bismuth collar designed to provide a transition from the circular shape of the cone to the square shape required to match with the lead shielding bricks comprising the final shield wall. The collar accommodates borated or lithiated polyethylene inserts to provide various beam aperture sizes and field shapes.

Neutron spectrum measurements for an imaginary transverse "source plane" passing through the base of the square flange on the downstream side of the bismuth collimator collar are summarized here. The source plane is a mathematical construct used for specifying the neutron source boundary conditions for the various dosimetry and treatment planning computations required to support each experimental irradiation. By definition, the physical beamline components upstream of the source plane do not change from one irradiation to the next. Components downstream of

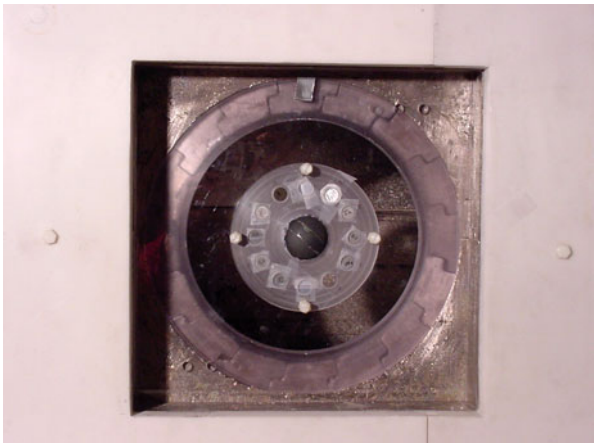

Fig. 13.5 Activation foil plate positioned in the WSU epithermal neutron beam source plane

Table 13.1 Activation interactions and foils used for the WSU epithermal neutron beam measurement example

Neutron interaction	Spectral modification	Energy range of primary response	Activation gamma energy of interest (keV)
^{197}Au (n, γ)	None	Thermal	411
^{115}In (n, γ)	Cadmium cover	1 eV resonance	1,293, 1,097, and 416
^{197}Au (n, γ)	Cadmium cover	5 eV resonance	411
^{186}W(n, γ)	Cadmium cover	18 eV resonance	686
^{55}Mn(n, γ)	Cadmium cover	340 eV resonance	847
^{63}Cu (n, γ)	Cadmium cover	1 keV resonance	511 (positron)
^{45}Sc(n, γ)	Cadmium cover	4.5 keV resonance	1,120, 889
^{115}In (n,n′)	Boron-10 shield	430 keV threshold	336

this plane, such as the field-shaping plates, can change for each irradiation and are therefore explicitly modeled in dosimetry and treatment planning computations. Time-consuming beam modeling computations are thus done only once for each beamline configuration upstream of the source plane, and the results are coupled to the patient dosimetry computations for each irradiation via a computed boundary condition specified for the source plane and validated by appropriate measurements such as described in this example.

Standard 12.7-mm (0.5") diameter In, Au, W, Mn, Cu, and Sc foils were used with a lexan foil positioning plate shown in Fig. 13.5. The neutron activation interactions and resulting gamma emissions of interest are listed in Table 13.1. These provide good coverage of the energy range of interest, but many other resonance and threshold interactions are available and are widely used [7, 31]. Cadmium covers are placed around some foils as indicated to suppress the thermal neutron response. Thus, each foil responds largely to neutrons having energies at or near the energy of the respective primary resonance of the foil material, as shown in the first six lines of Table 13.1. The covered foils were placed in outer foil positioning plate

positions. An uncovered gold foil was also placed in an outer position of the foil plate to measure the thermal flux. The foils had nominal thicknesses in the range of 0.0254 mm (0.001") to 0.127 mm (0.005"), depending on the material type.

An additional foil package is used to provide key spectral information in the energy range above epithermal ($E > 10$ keV). A heavy (~5 g) 25.4-mm diameter indium foil was placed in a small hollow boron sphere (inside diameter 2.8 cm, outside diameter 4.75 cm) located in the center of the foil positioning plate as can be seen in Fig. 13.5. The composition of the sphere is approximately 93 % ^{10}B and 7 % ^{11}B by weight, with a total boron density of 2.6 g/cm^3. This arrangement provides essentially total suppression of thermal *and* epithermal neutrons within the inner cavity of the boron sphere. Thus, an artificial threshold above the resonance neutron capture energy range for indium is imposed on the foil within the sphere. Since the activation gamma emissions that arise from neutron capture in indium are thereby suppressed, the relatively weak 336-keV gamma line from inelastic scatter in indium, which is of crucial interest in these measurements, is also much more prominent in the spectrum of the activated indium foil.

The irradiated foils used for this example were assayed at WSU using a standard high-purity germanium (HPGe) gamma spectrometry system (Canberra/Genie™). The induced activities in the foils were computed from the photopeak areas and system efficiencies based on calibration of the spectrometer using a National Institute of Standards and Technology (NIST)-traceable mixed europium-antimony calibration source. The measured activity of the heavy indium foil in the boron sphere was corrected for gamma self-shielding using an escape fraction at 336 keV calculated using a combination of MCNP computations and handbook data for the specific source-detector geometry that was used for the assay. This factor was 0.90 ± 0.01. The saturation activities of the various foils were then used to estimate the neutron spectrum by way of the overdetermined least-squares matrix unfolding procedure [43] discussed previously, with the required shielded foil cross sections computed using an MCNP model of the foil plate, the foils, and their surrounding spectral modification covers.

Figure 13.6 shows an unfolded 6-group free-field unperturbed neutron spectrum in the source plane, projected by the unfolding process (via the self-shielding factors) to the center of the foil positioning plate. The a priori 47-group neutron spectrum is also shown for comparison. The broad-group structure used for calculating the unfolded 6-group spectrum from the data for the eight activation interactions considered was selected to provide a well-conditioned unfolding matrix and to permit an accurate integration of the measured spectrum in the epithermal energy range to determine the total epithermal neutron flux. Integrating the measured curve over the epithermal energy range (0.5 eV–10 keV) produces a total epithermal neutron flux in the source plane of 1.66×10^9 n/cm^2-s at 1 MW with a propagated uncertainty of approximately 5 % (1σ).

A simple, but widely used, metric for the biophysical quality of reactor-based epithermal neutron beams is based on dividing the free-field neutron kerma rate of the beam (integrated over all energies above thermal) due to proton recoil by the useful epithermal neutron flux, again measured in the free field. This parameter is

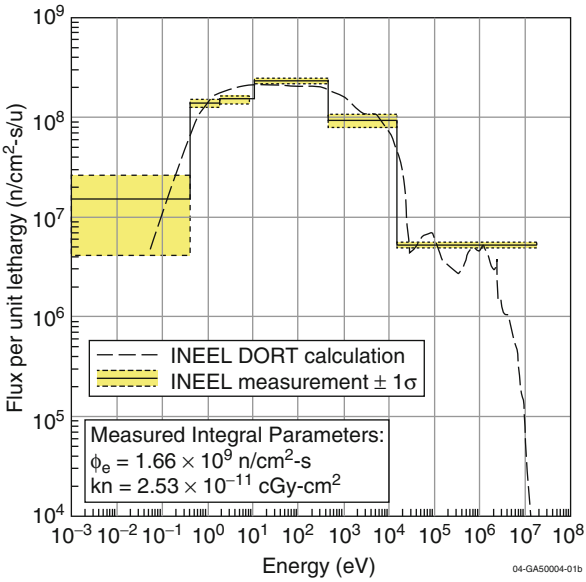

Fig. 13.6 Unfolded free-beam neutron spectrum in the source plane obtained by direct least-squares deconvolution for the WSU epithermal neutron beam facility. The reactor power is 1 MW

an indicator of the nonselective neutron background dose that will be produced in tissue by the above-thermal spectral component of the beam itself, in the absence of any neutron capture agent that may be administered to the patient. It is computed here for WSU using the measured flux spectrum in conjunction with broad-group kerma factors based on data for the components of standard tissue available on File 27 of the BUGLE [54] cross-section library. Fine-group neutron kerma factors are averaged over the broad unfolding group structure using the a priori spectrum as a weighting function to produce the necessary information. This procedure yields a measured free-beam spectral-average neutron kerma factor of 2.53×10^{-11} cGy total neutron kerma from all components per unit useful epithermal neutron flux, with an estimated uncertainty of about 7 %. This is in excellent agreement with the computed value of 2.75×10^{-11} cGy-cm^2.

Approximately 91 % of the direct background neutron dose from the WSU beam results from proton recoil. Additional background dose in tissue is of course produced by other nonselective, thermal-neutron-induced components, primarily neutron capture in nitrogen and hydrogen as noted earlier. These components are not directly indicative of the intrinsic biophysical quality of the incident beam. They must be taken into account in treatment planning, however, and are computed by folding the appropriate kerma factors with the measured spectrum in the same manner. The incident gamma component in the beam could also theoretically be measured by activation techniques (photoactivation of the ^{115}In isomer, e.g.), but this is not ordinarily done in BNCT practice for a number of reasons beyond the scope of this discussion.

Activation measurements are also widely used to characterize the neutron flux in various types of phantoms. Figure 13.7 shows a small polymethylmethacrylate (PMMA) phantom adjacent to a 10.16-cm beam aperture at WSU. Small segments

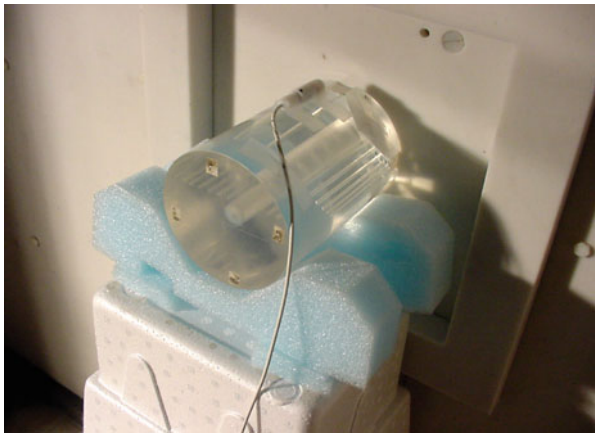

Fig. 13.7 Cylindrical PMMA phantom in the epithermal neutron beam at WSU. The diameter of the phantom is 12.5 cm and the length is 18.1 cm

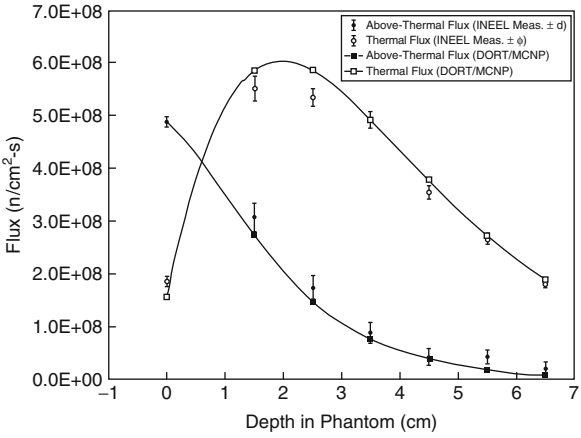

Fig. 13.8 Unfolded thermal and above-thermal flux along the central axis of a small PMMA phantom in the epithermal neutron beam at WSU. The horizontal axis corresponds to the distance downstream from the beam aperture plane

of copper wire containing 1.55 % gold by weight as placed on the axis of this phantom at various distances downstream from the aperture plane. Although copper has a weak resonance at about 1 keV, it is primarily sensitive to thermal neutrons, while gold is sensitive to both thermal and resonance neutrons, the latter primarily at about 5 eV. The gold and copper activation is measured simultaneously in each wire, and a two-group (thermal and above-thermal) spectrum can be unfolded from the data at each spatial location.

Figure 13.8 shows the results of the two-group spectral unfolding process for the phantom. Calculated and measured flux data are shown for comparison. Once the measured flux profiles are available, most of the significant BNCT dose components may be estimated as functions of depth in the phantom by application of appropriate spectrally averaged kerma factors as multipliers on the flux. The background hydrogen-recoil dose is essentially proportional to the above-thermal flux, while the nitrogen (n,p) dose and the boron neutron capture dose are proportional to the thermal

neutron flux. Neutron capture by hydrogen, which leads to emission of a 2.2 MeV gamma ray, is also proportional to the thermal flux, but the resulting photon source distribution is ordinarily used as input to a separate calculation of the photon dose that accounts for the fact that the source photons travel away from their initial locations prior to depositing significant radiation dose by the usual three mechanisms (photoelectric effect, Compton scattering, and pair production). The photon dose (both induced and incident) may also be measured directly by methods to be described in the following sections.

13.3 Gas-Filled Detectors

Various types of gas-filled radiation detectors have been successfully applied for measurement of the macrodosimetric properties of neutron sources for BNCT as well as for online beam intensity monitoring. The most important detector types that have been found useful for these applications are summarized in this section. These include ionization chambers, proton-recoil proportional counters, BF_3 and ^3He proportional counters, and fission chambers. Tissue-equivalent proportional counters, used primarily for microdosimetry, are not included here.

13.3.1 Ion Chambers

Paired ion chambers, one relatively more sensitive to neutrons and the other more sensitive to gammas, offer the most widely used method for online dosimetry of neutron sources used in BNCT. This approach provides additional information that complements what can be obtained from activation spectrometry and is in fact specifically recommended for separation of the incident gamma and neutron dose components in the "free" beam (i.e., the beam as it exits from the reactor or accelerator-based system used for neutron production and beam tailoring) as well as for measurements of the background neutron and gamma (incident and neutron-induced) dose components in standard water and tissue-equivalent plastic phantoms.

In general, ion chambers used for BNCT dosimetry should offer several design features that are important to this particular application [31]. The chamber size should be as small as possible, in order to minimize flux gradients across the active volume. The compositions of the wall and gas materials in the tissue-equivalent chamber should be the same as possible, and care should be taken so that the hydrogen and nitrogen contents are as close as possible to that of the tissue of interest. For example, A-150 plastic for the wall material is recommended as a good match to brain tissue. Minimum wall thickness for the tissue-equivalent chamber should be sufficient to provide charged-particle equilibrium for the most energetic recoil protons expected. The neutron-insensitive chamber should of course be constructed of materials with a minimum sensitivity to neutrons, especially in the thermal energy range. When used for in-phantom measurements, the wall thickness of

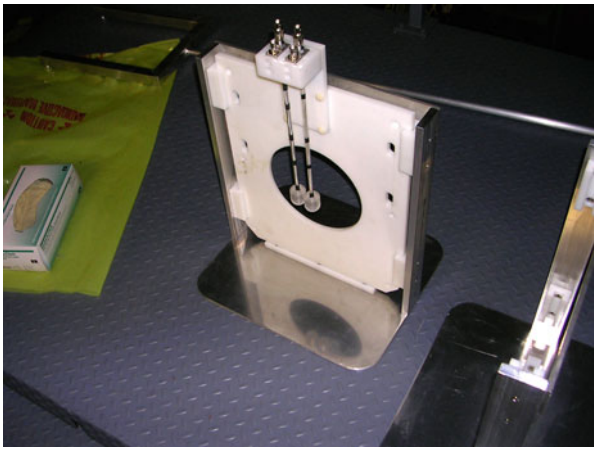

Fig. 13.9 Typical paired ion chambers used for BNCT dosimetry, with buildup caps in place for free-beam dosimetry

Fig. 13.10 Water phantom at WSU (*left*), with detail of paired ion chamber arrangement (*right*)

the neutron-insensitive chamber should be as thin as possible to minimize perturbation of the secondary electron fluence generated in the phantom.

Figure 13.9 shows a typical set of paired ion chambers, mounted on a lithiated polyethylene beam-shaping aperture plate that is used in the thermal neutron beam at the University of Missouri Research Reactor [15]. The active region of the gamma-sensitive chamber (FarWest™ IC-18) has a graphite wall with CO_2 gas. The neutron-sensitive chamber (FarWest™ IC-18 G) uses a tissue-equivalent gas (64.4 % CH_4, 32.5 % CO_2, and 3.1 % N_2 by volume) and a wall of tissue-equivalent plastic (e.g., A-150). The active volume of each of these chambers is 0.1 ml. Magnesium chambers with argon gas can also be used for the gamma measurement. Figure 13.10 shows the same chambers positioned in a standard water phantom at Washington State University [44].

These chambers feature several sophisticated details in their construction and operation. There is, for example, a grounded guard ring to bleed off leakage current between the actual active chamber region (a sphere at the tip of the long cylindrical stem) and the collection electrode. The chambers are connected to standard

electrometers and produce currents in the range of a few picoamperes in mixed neutron-gamma fields typical of BNCT applications. They typically operate with a bias voltage of 250 VDC, which for practical purposes is sufficient to achieve saturation. Low-noise cables should be used, and care should be taken to keep the cable out of the radiation field as much as possible to minimize spurious radiation-induced currents originating from locations other than in the chamber itself.

Ion chambers are initially calibrated by the manufacturer in a standard gamma field. For example, the IC-18G shown in the figures has a calibration of 1.64×10^{10} R/Coloumb. The corresponding tissue-equivalent chamber (IC-18) has a calibration of 2.25×10^{10} R/C. The chambers are calibrated for a standard gas flow rate, typically 5 ml/min at a specified gas pressure and temperature, typically 22 °C and 760 mm. Appropriate adjustments to the calibration are required if the gas conditions are not as stated in the calibration data. Use of buildup caps for measurements of the beam in air is generally recommended.

The responses of paired ion chambers may be characterized by the following two equations, which are solved simultaneously to determine the neutron and gamma doses:

$$N_u Q_u = h_u D_g + k_u D_n - t_u \varphi_{th} \tag{13.9}$$

$$N_t Q_t = h_t D_g + k_t D_n - -t_t \varphi_{th} \tag{13.10}$$

where:

D_g and D_n are the gamma- and neutron-absorbed doses in the reference material corresponding to the calibration (typically air or water).

N_u and N_t are the calibration factors (R/C) for the chambers for the neutron-insensitive and the tissue-equivalent chambers, respectively. Calibration data are generally provided by the manufacturer and may be used directly for beam design confirmation and preclinical dosimetry. *However, it is important to recognize that these factors must be independently confirmed against traceable standards in the case of clinical applications, as described elsewhere.*

Q_u and Q_t are the charges collected by the chambers, corrected for charge recombination (usually negligible) and for local temperature and air pressure as specified by the manufacturer.

h_u and h_t are the sensitivities of the chambers to the gamma radiation of interest relative to the sensitivities to the gamma field used for calibration and may be determined by any standard method that includes the effect of gamma spectral differences and, ideally, the local gamma field spatial perturbation by the chambers.

k_u and k_t are the sensitivities of the chambers to the neutron field of interest relative to the sensitivities to the gamma field used for calibration.

t_u and t_t are the sensitivities of the chambers per unit thermal neutron fluence.

ϕ_{th} is the thermal neutron fluence at the measurement location.

Determination of the sensitivities of the chambers to the neutron field of interest relative to the sensitivities to the gamma field used for calibration can be somewhat

complicated and application dependent. Useful information can be found in ICRU-26 [28] and ICRU-45 [29]. Typical values of relative neutron sensitivity for neutron-insensitive chambers range from zero to approximately 0.15, depending on details of the chamber construction and the specific application. Typical values for the tissue-equivalent chamber range from 0.9 to 1.4, depending again on the details of the chamber and on the application, as well as on the details of the correction for nitrogen (n,p) interactions. A complete discussion of these factors and their specific determination is beyond the scope of this chapter. Additional practical details on this subject, as well as on other key aspects of the paired ion chamber technique, are available in Rogus et al. [53], Raaijmakers et al. [47, 48], Kosunen et al. [35], and Roca et al. [52].

Paired ion chamber readings must be corrected to reflect dose in the reference tissue of interest relative to the response of the medium (e.g., a water phantom) used for beam characterization. In the case of the neutron-insensitive chamber, this is typically done using the ratio of the mass attenuation coefficients of the reference tissue relative to that of the phantom material, averaged over the gamma spectrum obtained from a calculation or perhaps from an actual spectral measurement. In the case of the tissue-equivalent chamber, the correction may be calculated using ratios of the neutron kerma factors for the two materials, averaged over the neutron spectrum.

Finally, the third terms on the right-hand side of Eqs. 13.9 and 13.10 are required to correct for thermal-neutron-induced dose to the chambers that is not characteristic of the tissue of interest. This is especially important in the case of the tissue-equivalent chamber since a significant component of its response results from the nitrogen (n,p) interaction, and the nitrogen content of the chamber wall and fill gas is not necessarily equivalent to that of the tissue of interest, which varies considerably (as much as a factor of 2) from one tissue type to another. The thermal neutron response of the chambers is typically computed using the thermal neutron flux determined by activation spectrometry as described previously, folded with the appropriate kerma factors for the chamber materials. Online measurement (e.g., [8]) can also be used to determine the chamber response of interest. In the case of of Eqs. 13.9 and 13.10, this response is subtracted from the chamber readings. The background dose to the tissue due to thermal-neutron-induced high-LET interactions such as (n,p) is then computed for the appropriate tissue composition and reported separately. Other, equivalent, mathematical formulations for the thermal neutron correction are also possible.

13.3.2 BF_3 and ^3He Detectors

The utility of these detectors is based on the fact that ^{10}B and ^3He have large cross sections for low-energy neutron capture with subsequent emission of energetic charged particles whose energy appears as collected charge in a suitable gas-filled tube [6, 33]. In the case of boron trifluoride, the emitted particles are lithium and helium ions, just as with the BNCT interaction in tissue. In the case of

^{3}He, energetic protons and tritons are released. These detectors are generally operated as proportional counters in pulse mode, allowing for discrimination against gamma radiation, but they do not generally provide any significant information about the energy of the incident neutrons. This type of detector, especially with boron trifluoride as the fill gas, has been found useful for online neutron beam monitoring and for thermal neutron measurements in various phantom and in vivo applications (see, e.g., [1, 58]).

13.3.3 Proton-Recoil Spectrometers

Recoil detectors for neutrons employ tubes filled with low molecular weight gasses (typically hydrogen or helium) at pressures up to a few atmospheres. Gas atoms that are elastically scattered by incident neutrons in the energy range where this type of detector is useful will be stripped of their electrons and will have sufficient energy to create many ion pairs in the surrounding gas as they slow down. The collected charge associated with each neutron scattering event will be proportional to the initial energy of the scattered ion. In the case of hydrogen-filled detectors, which have been the most popular for BNCT applications and therefore will be the primary subject of discussion here, the recoil proton spectrum bears a particularly simple relationship to the energy of the incident neutron. This is because (1) neutrons and protons have essentially the same mass and (2) elastic scattering of neutrons by hydrogen may be assumed to be isotropic in the center of mass system for neutrons having energies of interest in BNCT applications. As a result, it can be shown that the energy spectrum of the recoiling protons is constant with respect to energy, over the range from essentially zero up to the energy of the incident neutron. Furthermore, the elastic scattering cross section of hydrogen for neutrons in the energy range of interest for BNCT is also constant with respect to energy, facilitating the spectral unfolding process as described below.

Proton-recoil tubes are operated as proportional counters, in pulse mode. This typically requires that the neutron source of interest be operated at a much lower flux level for this type of measurement than is the case with actual clinical application. The measurements must thus be scaled to the full operating flux level, with any nonlinearity in the scaling factor properly accounted for. Each neutron scattering event in the detector gas produces a recoil proton. The ionization energy deposited in the gas by this proton appears as collected charge per pulse, and the signal is stored in the appropriate bin of a suitable multichannel analyzer. A proton-recoil spectrum is thus constructed, and the incident neutron spectrum may be unfolded from this spectrum using mathematical techniques based on the previously described relationship between the incident neutron energy and the recoil-proton energy spectrum. Basically, the magnitude of the proton-recoil spectrum at a given energy is proportional to the integral of all neutron scattering events that have occurred at this energy and above, and the incident neutron spectrum can in principal be obtained by simple differentiation of the recoil-proton spectrum. Energy calibration of the detector may be facilitated by the addition of a trace quantity of

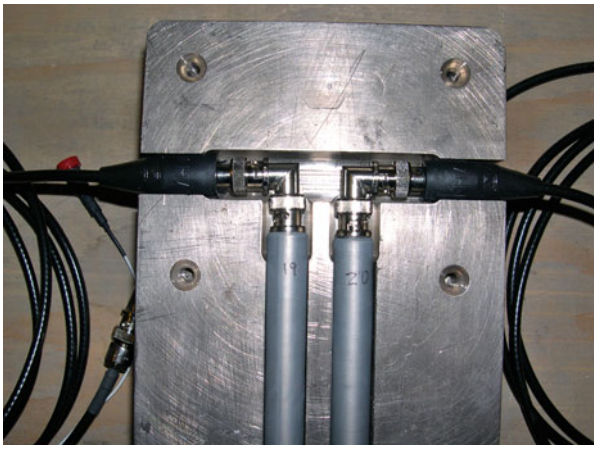

Fig. 13.11 Fission chambers used for beam monitoring at the Washington State University epithermal neutron beam facility (Reuter-Stokes Model P6-0402-101)

a suitable gas (e.g., nitrogen or ^{3}He) that exhibits a neutron capture reaction with emission of a proton or other charged particle with a known energy.

Although proton-recoil chamber counters can theoretically be used to detect neutrons of any energy, there are complications that limit their practical utility to the range of approximately 10 keV to typically a few MeV, and various corrections to the data are required. In the lower part of the useful energy range (10 keV up to approximately 100 keV for most devices), significant corrections must be made to separate the inevitable incident gamma content of essentially all neutron sources that are used for BNCT. These corrections can be made to some extent by direct subtraction if the absolute magnitude of the gamma contamination is known, and suitable gamma sources with spectra that are similar to that of the gamma content of the beam are available. Pulse-shape discrimination can also be used in the lowest part of the energy range to separate the gamma component, at the expense of somewhat more complicated electronics. In the higher parts of the energy range, corrections must be made for the fact that recoil protons may travel all of the way to the wall of the chamber without depositing all of their energy in the gas (the so-called wall effect). The correction for this effect is dependent on the pressure of the fill gas. As with all proportional counters, great care must be taken to avoid contamination of the fill gas with air, which would interfere with the charge multiplication process. A number of other considerations and precautions that must be observed in connection with the use of proton-recoil chambers, in general and specific to BNCT, are discussed in the literature [26, 33, 45].

13.3.4 Fission Chambers

Fission chambers used for BNCT applications generally take the form of small cylindrical tubes (Fig. 13.11) with a deposit of a fissionable nuclide on the inner surface. The fissionable material can be selected to permit detection of

fast neutrons, thermal neutrons, or both. They are used primarily as online beam intensity monitors, operated in current mode, but can also be operated in pulse mode, allowing discrimination of gamma radiation. A typical fission chamber used for BNCT has a small deposit (few milligrams) of ^{235}U on its inner surface and is therefore sensitive to low-energy neutrons. Typical fill gasses include argon or methane. Incident neutrons induce fissions in the uranium deposit, and the resulting fission fragments that travel into the gas cause ionization, and the resulting charge is collected and measured. The uranium deposit on the inner surface of the chamber may also include an appropriate quantity of ^{234}U as well to compensate for depletion of the ^{235}U during operation, especially if the chamber is to be used continuously.

Although the manufacturers of fission chambers generally provide calibration data, it is essential that fission chambers used for BNCT be calibrated for their specific application and their location in the neutron beamline relative to the source plane and the irradiation location. Calibration is typically accomplished via neutron activation spectrometry. Unlike self-powered neutron detectors (see Sect. 4.6), fission chambers conveniently provide an essentially immediate indication of any change in neutron beam intensity caused, for example, by the intentional closing of a beam shutter or by an unexpected change in reactor power or accelerator operating parameters.

13.4 Additional Techniques

Activation spectrometry and various gas-filled detectors have been the primary workhorses for neutron beam dosimetry and monitoring in BNCT. However, several additional radiation detection technologies, especially thermoluminescent dosimeters, have also been adapted for BNCT purposes and are used by various institutions and researchers for both beam characterization and some aspects of clinical dosimetry. The most prominent of these are described briefly in the following sections.

13.4.1 Scintillators

In the simplest sense, scintillation detectors are based on the emission of fluorescent light due to the excitation of atomic and molecular energy levels in the detector medium by ionizing radiation [33]. Scintillators may be in liquid or solid form and can be designed for measurement of neutrons or gammas. Inorganic crystals such as NaI and LaBr are widely used for radiation detection and spectrometry but have not seen significant use for direct beam characterization and dosimetry in BNCT. However, solid organic scintillators have been found useful. These may be in the form of pure organic crystals (e.g., anthracene, stilbene), or polymerized plastics (e.g., styrene, polyvinyl toluene, polymethylmethacrylate). Materials that feature a strong proton-recoil response are used for fast-neutron detection and spectrometry in BNCT, with the gamma response suppressed by pulse-shape discrimination.

Fig. 13.12 Thermoluminescent dosimeters arranged on a hamster phantom used for preclinical BNCT radiobiological studies [46]

Unfolding of the neutron flux from the recoil proton spectrum can in principal be accomplished by the same basic techniques as are used for gas-tube proton-recoil spectrometry although additional complications exist [31]. A boron compound can also be included in the scintillator, and the resulting signal is then largely proportional to the boron interaction rate at the measurement location. Applications of scintillators to BNCT are further described by Crawford et al. [18] and Ishikawa et al. [30]. Applications of scintillation in optical fibers have also been explored by Bliss et al. [13].

13.4.2 Thermoluminescent Dosimeters

In contrast to the types of scintillators described above, which emit a pulse of light essentially immediately after the deposition of radiation from a charged particle, thermoluminescent dosimeters (TLD) are designed to store the energy of the radiation in their solid crystal lattice until a later time, when the integrated energy, which is proportional to the radiation dose, is released by heating the dosimeter to a prescribed temperature. This design feature is accomplished by addition of so-called activator impurities that act as electron and hole trapping centers. The trapped charged carriers then recombine and produce optical photons when they are released by the heating process. Detailed descriptions of TLD physics are available in standard texts [6, 33].

Typical TLD materials include $CaSO_4$ with Mn added as an activator ($CaSO_4$:Mn), as well as CaF_2:Mn and LiF:Mn,Ti). LiF-based TLDs have seen the most use for BNCT applications. They are nearly tissue-equivalent and relatively inexpensive so that many measurements can be made at different locations in a phantom or in vivo subject (e.g., as in Fig. 13.12). Also, it is in principle possible to separate the neutron and gamma components of a mixed radiation field using lithium-based TLDs because they can be made sensitive primarily to neutrons through the use of enriched ^{6}Li (TLD-600), or

relatively insensitive to neutrons by use of ^{7}Li (TLD-700), although in the latter case, the neutron sensitivity cannot be completely eliminated and must be carefully accounted for in the analysis. Natural lithium LiF TLDs (TLD-100) are also available. Another type of lithium-based TLD that has been investigated for BNCT applications features a combination of Mg, Cu, and P as the activator and may offer somewhat improved capabilities for clean separation of neutron and gamma dose components.

A lengthy description of TLD applications and techniques in BNCT is beyond the scope of this chapter. The handling, calibration, and readout processes are complicated, but useful results can generally be produced with careful attention to detail. Excellent sources of additional information on BNCT-specific TLD applications include Järvinen and Voorbrack [31], Aschan et al. [3–5], Bilski et al. [9], Burn et al. [16], Croft and Perks [19], Kessler et al. [32], Konijnenberg et al. [34], Raaijmakers et al. [47, 48], Seppälä et al. [56], and Toivonen et al. [59].

13.4.3 Gel Detectors

Applications of Fricke dosimetry in tissue-equivalent gels have been explored as a possible means of two- and three-dimensional dosimetry in BNCT. In Fricke dosimetry, ferrous ions (Fe^{2+}) in a suitable medium (solution or gel) are converted to ferric (Fe^{3+}) ions through a complex series of chemical interactions that are induced by ionizing radiation. In the case of BNCT, gel detectors offer the possibility of three-dimensional dosimetry via, for example, irradiation of gel-based phantoms and subsequent imaging of the iron ion distribution using magnetic resonance imaging, whereby ferric and ferrous ions produce different perturbations of the proton relaxation rates in the medium [22]. Optical absorption imaging of the irradiated gel to quantify the dose distribution is also possible [23, 24].

13.4.4 Superheated Nucleation Detectors

The neutron activation approach for beam spectrometry is relatively simple and capable of very high accuracy in the energy ranges where many materials with linearly independent activation responses are available. However, it has a significant disadvantage when additional detail is desired for neutrons in the biologically important energy range of 10 keV to about 400 keV. Convenient materials with suitable characteristic activation responses (either resonance or threshold) are not readily available for detailed measurements in this radiobiologically important range of the neutron spectrum, just above the upper epithermal cutoff energy range. Other methods are available as noted elsewhere, but for the most part these also have their characteristic disadvantages. However, one promising low-cost alternate technique for this energy range is based on counting of radiation-induced nucleation sites in specialized superheated materials [2, 42].

An example of the implementation of this technique is provided by the RemSpec™ superheated drop detector (SDD) spectrometer. SDD dosimeter materials that are

Fig. 13.13 RemSpec superheated nucleation spectrometer unit positioned in the source plane at WSU

totally photon insensitive can be used with this device. These materials have thresholds for neutron detection between 50 keV and 1 MeV in the case of one medium and 500 keV to 10 MeV in the case of a second medium. In each case, the threshold energy can be fine-tuned by varying the temperature of the medium, and the response function of the medium above the threshold can be quantified. The RemSpec incorporates an SDD-containing vial, a temperature control system, and an acoustic sensor that records the formation of each nucleation site in real time, along with appropriate control and data acquisition software. Since the threshold and the response function of the SDD media are known at each temperature, it is possible to unfold the bubble formation data to produce a measured neutron spectrum within the energy range over which the medium is sensitive.

Figure 13.13 shows a RemSpec detector assembly positioned in the source plane of the previously described WSU beam. The actual detector material is enclosed in a tube that is incorporated into an insulated heating unit to vary the temperature as discussed above. An ion chamber is also suspended in the beam to provide an indication of the gamma dose rate in the free beam. The reactor power for the irradiation described here is on the order of a few tens of watts, in order to maintain a count rate within the specifications of the instrument.

Figure 13.14 shows some results from the RemSpec measurements. In this case, the fluxes are plotted on an expanded scale to show detail above about 30 keV, the lower threshold of the energy range that is detectable by this particular instrument. To obtain the results shown in this figure, the RemSpec detector response curves provided by the manufacturer were digitized to an 84-group equal-lethargy structure covering the energy range from 30 keV to 10 MeV. The a priori flux from the baseline beam design computations was likewise remapped into this same group structure. The spectrum implied by the RemSpec responses was estimated using a variation of the Sand-II empirical adjustment method [38] as described by Draper [20]. The measured results are normalized to a reactor power of approximately 300 kW in this particular case. The adjustment procedure produces a somewhat harder measured

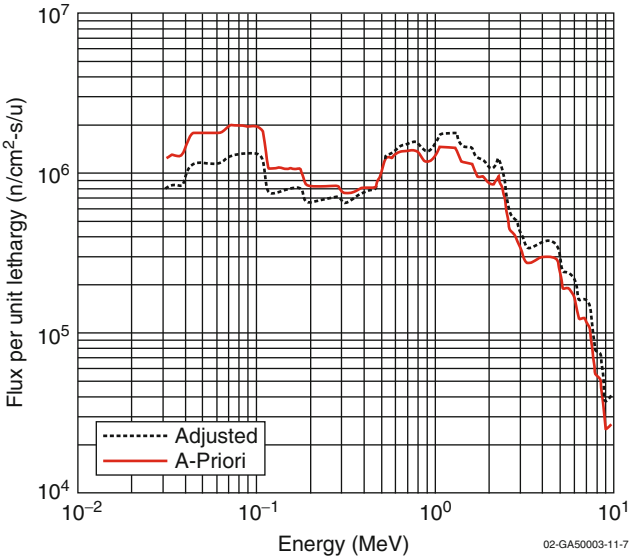

Fig. 13.14 Results of the RemSpec superheated nucleation detector measurements for the WSU epithermal neutron beam

spectrum compared to the a priori curve as seen in Fig. 13.14. Neutrons are shifted to the energy range above about 500 keV in order to produce the best fit to the observed detector responses.

13.4.5 Semiconductor Detectors

Semiconductors, which operate on the principle of electron–hole creation by radiation deposition, followed by pulse mode collection of the resulting current from each interaction, offer several advantages as radiation detectors and spectrometers. Their solid physical form provides significantly greater efficiency than gas-filled detectors, and the relatively low energy that is required to produce an electron–hole pair results in improved energy resolution compared to plastic or organic crystal scintillators. Germanium semiconductor detectors are of course very widely used for general high-resolution gamma spectrometry. These have been successfully applied for in-phantom monitoring of the 480 keV gamma that is produced by the boron-neutron interaction and the 2.2 MeV hydrogen capture gamma, yielding a viable method for monitoring of these dose components of BNCT therapy in vivo as well [62]. Silicon detectors alone, or with ^{10}B, ^{6}Li, or ^{235}U coatings that absorb neutrons to produce charged particles that subsequently create the detector signal, have also been used for neutron beam characterization [37] and as thermal neutron flux monitors in BNCT [25, 27, 36].

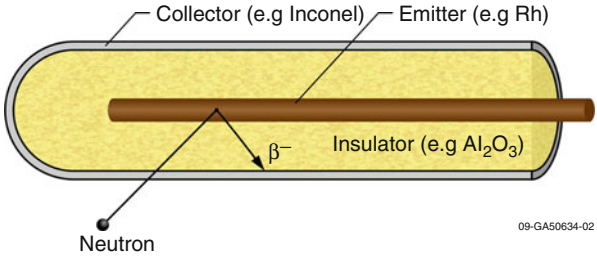

Fig. 13.15 Basic self-powered neutron detector design and operation

13.4.6 Self-Powered Neutron Detectors

Self-powered neutron detectors (SPND), or Hilborn detectors, offer a simple and robust method for online monitoring of neutron flux during BNCT irradiations. The basic principle of operation is illustrated in Fig. 13.15. A central electrode composed of a suitable metal with a relatively high neutron capture cross section is positioned within a surrounding cylindrical electrode, separated by an insulating material. In the most commonly employed mode of SPND operation, neutrons are captured in the central electrode, or emitter. Subsequent beta decay of the activation product produces energetic electrons that travel through the insulator to the outer electrode, producing a current in an external circuit. At equilibrium, this current is proportional to the neutron capture rate, and hence the neutron flux, at the location of the emitter.

Other interactions can also occur in an SPND and must be properly accounted for in the calibration process. These include prompt gamma production in the emitter and other structural materials, with subsequent Compton scatter of electrons that contribute to the detector current as well as production of electron currents via direct gamma interactions in the detector materials in the case of mixed neutron-gamma fields. Neutron and gamma interactions in the connection cable can also be significant and must be properly accounted for or canceled by suitable design of the external circuit.

Typical SPND emitter materials include vanadium and rhodium (Knoll 1999). Vanadium offers a lower sensitivity and is more suitable for measurements in high-flux fields typical of nuclear power reactors, whereas rhodium has a higher neutron cross section and corresponding higher sensitivity for neutron fluxes typical of BNCT (in the range of 10^9–10^{10} n/cm^2-s). Rhodium also has a shorter half-life for its most prominent beta decay mode, allowing equilibrium to be reached more quickly.

Miller et al. [39] have developed an implantable rhodium-zircaloy SPND that has proven useful for beam monitoring [15] as well as for in vivo neutron dosimetry [21]. This detector has an active length of 10 mm with an unusually small outer collector diameter of 2 mm to facilitate in vivo applications. Neutron calibration is typically accomplished by comparison with foil or wire neutron activation measurements.

Acknowledgments Preparation of this article was supported in part via a faculty-staff exchange grant administered by the Idaho National Engineering Laboratory under Battelle Energy Alliance, LLC contract no. DE-AC07-05ID14517 with the US Department of Energy. The author would also like to acknowledge Mr. Stuart Slattery, University of Wisconsin, for his assistance in compilation of the extensive bibliography that is presented here.

References

1. Alburger DE, Raparia D, Zucher MS (1999) Phantoms with $^{10}BF_3$ detectors for boron neutron capture therapy applications. Med Phys 25:1735–1738
2. Apfel RE, Lo Y-C (1979) Practical neutron dosimetry with superheated drops. Health Phys 56:79–83
3. Aschan C, Toivonen M, Savolainen S, Seppälä T, Auterinen I (1999) Epithermal neutron beam Dosimetry with thermoluminescence dosimeters for boron neutron capture therapy. Radiat Prot Dosimetry 81:47–56
4. Aschan C, Toivonen M, Savolainen S, Stecher-Rasmussen F (1999) Experimental correction for thermal neutron sensitivity of gamma ray TL dosimeters irradiated at BNCT beams. Radiat Prot Dosimetry 82:65–69
5. Aschan C, Lampinen JS, Savolainen S, Toivonen M (1999) Monte Carlo simulation of the influence of adjacent TL dosimeters on TL readings in simultaneous measurements in BNCT beams. Radiat Prot Dosimetry 85:349–352
6. Attix FH (1986) Introduction to radiological physics and radiation dosimetry. Wiley, New York
7. Auterinen I, Serén T, Uusi-Simola J, Kosunen A, Savolainen S (2004) A toolkit for epithermal neutron beam characterization in BNCT. Radiat Prot Dosimetry 110:587–593
8. Becker J, Brunckhorst E, Roca A, Stecher-Rasmussen F, Moss R, Böttger R, Schmidt R (2007) Setup and calibration of a triple ionization chamber system for dosimetry in mixed neutron/photon fields. Phys Med Biol 52:3715–3727
9. Bilski P, Budzanowski M, Ochab E, Olko P, Czopyk L (2004) Dosimetry of BNCT beams with novel thermoluminescent detectors. Radiat Prot Dosimetry 110:623–626
10. Binns PJ, Riley KJ, Harling OK, Kiger WS III, Munck af Rosenschöld PM, Giusti V, Capala J, Sköld K, Auterinen I, Serén T, Kotiluoto P, Uusi-Simola J, Marek M, Viererbl L, Spurny F (2005a) An international dosimetry exchange for boron neutron capture therapy, part 1: absorbed dose measurements. Med Phys 32:3729–3736
11. Binns PJ, Riley KJ, Harling OK (2005b) Epithermal neutron beams for clinical studies of boron neutron capture therapy: a dosimetric comparison of seven beams. Radiat Res 64:212–220
12. Blaumann HR, Gonzalez SJ, Longhino J, Santa Cruz GA, Calzetta Larrieu OA, Bonomi MR, Roth BMC (2004) Boron neutron capture therapy of skin melanomas at the RA-6 reactor: a procedural approach to beam setup and performance evaluation for upcoming clinical trials. Med Phys 31:70–80
13. Bliss M, Craig RA, Sunberg DS, Harker YD, Hartwell JK, Venhuizen JR (1997) Progress towards development of real-time dosimetry for BNCT. In: Larsson B, Crawford J, Weinrich R (eds) Advances in neutron capture therapy, vol I, Medicine and physics. Elsevier Science BV, Amsterdam
14. Breismeister JF (1993) MCNP – a general Monte Carlo N-particle transport code, Version 4A, LA-12625-M. Los Alamos National Laboratory, Los Alamos
15. Brockman J, Nigg DW, Hawthorne MF, McKibben C (2009) Spectral performance of a composite single-crystal filtered thermal neutron beam for BNCT research at the University of Missouri. Appl Radiat Isot 67:S222–S225
16. Burn KW, Colli V, Curzio G, d'Errico F, Gambarini G, Rosi G, Scolari L (2004) Characterization of the tapiro BNCT epithermal facility. Radiat Prot Dosimetry 110:645–649
17. Coderre JA, Morris GM (1999) The radiation biology of boron neutron capture therapy. Radiat Res 151:1–18

18. Crawford JF, Teichmann S, Stecher-Rasmussen F (1996) A direct comparison of neutron energy spectra at high and low powers in the HB11 beam at HFR Petten. In: Mishima Y (ed) Cancer neutron capture therapy. Plenum Press, New York
19. Croft S, Perks CA (1990) Corrections to gamma ray dosimetry measurements made in Harwell's two high-intensity filters neutron beams using ^{7}LiF thermoluminescent dosimeters owing to their neutron sensitivity. Radiat Prot Dosimetry 33:351–354
20. Draper EL Jr (1971) Integral reaction rate determinations – part I: tailored reactor spectrum preparation and measurement. Nucl Sci Eng 48:22–30
21. Gadan M, Crawley V, Thorp S, Miller M (2009) Preliminary liver dose estimation in the new facility for biomedical applications at the RA-3 reactor. Appl Radiat Isot 67:5206–5209
22. Gambarini G, Birattari C, Colombi C, Pirola L, Rosi G (2002) Fricke gel dosimetry in boron neutron capture therapy. Radiat Prot Dosimetry 101:419–422
23. Gambarini G, Colli V, Gay S, Petrovich C, Pirola L, Rosi G (2004) In-phantom imaging of all dose components in boron neutron capture therapy by means of gel dosimeters. Appl Radiat Isot 61:759–763
24. Gambarini G, Daquino GG, Moss RL, Carrara M, Nievaart VA, Vanossi E (2007) Gel dosimetry in the BNCT facility for extra-corporeal treatment of liver cancer at the HFR Petten. Radiat Prot Dosimetry 126:604–609
25. Harasawa S, Nakamoto A, Hayakawa Y, Egawa J, Aizawa O, Nozaki T, Minobe T, Hatanaka H (1981) Improved monitoring system of neutron flux during boron neutron capture therapy. Radiat Res 88:187–193
26. Harker YD, Anderl RA, Becker GK, Miller LG (1992) Spectral characterization of the epithermal neutron beam at the Brookhaven medical research reactor. Nucl Sci Eng 110:355–368
27. Hayakawa Y, Harasawa S, Nakamoto A, Amano K, Hatanaka H, Egawa J (1978) Simultaneous monitoring system of thermal neutron flux for boron neutron capture therapy. Radiat Res 75: 243–251
28. ICRU Report 26 (1977) Neutron dosimetry for biology and medicine. International Commission on Radiation Units and Measurement, Bethesda
29. ICRU Report 45 (1989) Clinical neutron dosimetry part 1: determination of absorbed dose in a patient treated by external beams of fast neutrons. International Commission on Radiation Units and Measurement, Bethesda
30. Ishikawa M, Ono K, Sakurai Y, Unesaki H, Uritani A, Bengua G, Kobayashi T, Tanaka K, Kosako T (2004) Development of real-time thermal neutron monitor using boron-loaded plastic scintillator with optical fiber for boron neutron capture therapy. Appl Radiat Isot 61:775–779
31. Järvinen H, Voorbraak WP (2003) Recommendations for the dosimetry of boron neutron capture therapy, Report 21425/03 55339/C, NRG Petten
32. Kessler C, Stecher-Rasmussen F, Rassow J, Garbe S, Sauerwein W (2001) Application of thermoluminescent dosimeters to mixed neutron-gamma dosimetry for BNCT. In: Hawthorne MF et al (eds) Frontiers in neutron capture therapy, vol 2. Kluwer Academic/Plenum Publishers, New York, pp 1165–1173
33. Knoll GF (2000) Radiation detection and measurement, 3rd edn. Wiley, New York
34. Konijnenberg MW, Raaijmakers CPJ, Dewitt L, Mijnheer BJ, Moss RL, Stecher-Rasmussen F, Watkins PRD (1992) Treatment planning of boron neutron capture therapy: measurements and calculations. Radiat Prot Dosimetry 44:443–446
35. Kosunen A, Kortesniemi M, Ylä-Mella H, Seppälä T, Lampinen J, Serén T, Auterinen I (1999) Twin ionization chambers for dose determinations in phantom in an epithermal neutron beam. Radiat Prot Dosimetry 81:187–194
36. Litovchenko PG, Moss R, Stecher-Rasmussen F, Appelman K, Barabash LI, Kibkalo TI, Lastovetsky VF, Litovchenko AP, Pinkovska MB (1999) Semiconductor sensors for dosimetry of epithermal neutrons, semiconductor physics. Quantum Opt Optoelectronics 2:90–91
37. Marek M, Viererbl L, Burian J, Jansky B (2001) Determination of the geometric and spectral characteristics of BNCT beam (neutron and gamma ray). In: Hawthorne F, Shelly K, Wiersema R (eds) Frontiers in neutron capture therapy. Kluwer Academic/Plenum Publishers, New York

38. McElroy WN, Berg S (1967) SAND-II neutron flux spectra determination by multiple foil activation iterative method. AWRL-TR-67-41, vol 1–4
39. Miller M, Mariani LE, Sztejnberg Gonçalves-Carralves ML, Skumanic M, Thorp S (2004) Implantable self-powered detector for online determination of neutron flux in patients during NCT treatment. Appl Radiat Isot 61:1033–1037
40. Moss RL, Stecher-Rasmussen F, Rassow J, Morrissey J, Voorbraak W, Verbakel W, Appelman K, Daquino GG, Muzi L, Wittig A, Bourhis-Martin E, Sauerwein W (2004) Procedural and practical applications of radiation measurements for BNCT at HFR Petten. Nucl Instrum Methods Phys Res B 213:633–636
41. Munck af Rosenschöld PM, Giusti V, Ceberg CP, Capala J, Sköld K, Persson BRR (2003) Reference dosimetry at the neutron capture therapy facility at Studsvik. Med Phys 30: 1569–1579
42. Nath R, Meigooni C, King C, Smolen S, d'Errico F (1993) Superheated drop detector for determination of neutron dose equivalent to patients undergoing high-energy X-ray and electron radiotherapy. Med Phys 20:78
43. Nigg DW, Wemple CA, Risler R, Hartwell JK, Harker YD, Laramore GE (2000) Modification of the University of Washington neutron radiography facility for optimization of neutron capture enhanced fast-neutron therapy. Med Phys 27:359–367
44. Nigg DW, Venhuizen JR, Wemple CA, Tripard GE, Sharp S, Fox K (2004) Flux and instrumentation upgrade for the epithermal neutron beam facility at Washington State University. Appl Radiat Isot 61:993–998
45. Perks CA, Gibson AB (1992) Neutron spectrometry and dosimetry for boron neutron capture therapy. Radiat Prot Dosimetry 44:425–428
46. Pozzi E, Nigg DW, Miller M, Thorp SI, Heber EM, Zarza L, Estryk G, Monti Hughes A, Molinari AJ, Garabalino M, Itoiz ME, Aromando RF, Quintana J, Trivillin VA, Schwint AE (2009) Dosimetry and radiobiology at the new RA-3 reactor boron neutron capture therapy (BNCT) facility: application to the treatment of experimental oral cancer. Appl Radiat Isot 67:S309–S312
47. Raaijmakers CPJ, Konijnenberg MW, Verhagen HW, Mijnheer BJ (1995) Determination of dose components in phantoms irradiated with an epithermal neutron beam for boron neutron capture therapy. Med Phys 22:321–329
48. Raaijmakers CPJ, Watkins PRD, Nottelman EL, Verhagen HW, Jansen JTM, Zoetelief J J, Mijnheer BJ (1996) The neutron sensitivity of dosimeters applied to boron neutron capture therapy. Med Phys 23:1581–1589
49. Rhoades WA, Childs RL (1988) The DORT two-dimensional discrete-ordinates transport code. Nucl Sci Eng 99:88–89
50. Riley KJ, Binns PJ, Harling OK, Kiger WS III, Gonzalez SJ, Casal M, Longhino J, Calzetta Larrieu OA, Blaumann HR (2008) Unifying dose specification between clinical BNCT centers in the Americas. Med Phys 35:1295–1298
51. Riley KJ, Binns PJ, Harling OK, Albritton JR, Kiger WS III, Rezaei A, Sköld K, Seppälä T, Savolainen S, Auterinen I, Marek M, Viererbl L, Nievaart VA, Moss RL (2008) An international dosimetry exchange for BNCT part II: computational dosimetry normalizations. Med Phys 35:5419–5425
52. Roca A, Nievaart VA, Moss RL, Stecher-Rasmussen F, Zamfir NV (2007) Validating a MCNPX model of Mg(Ar) and TE(TE) ionization chambers exposed to ^{60}Co gamma rays. Radiat Prot Dosimetry 129:365–371
53. Rogus RD, Harling OK, Yanch JC (1994) Mixed field dosimetry of epithermal neutron beams for boron neutron capture therapy at the MITR-II research reactor. Med Phys 21:1611–1625
54. Roussin RW (1980) BUGLE-80 coupled 47-neutron, 20 gamma-ray P3 cross section library, DLC-75. Radiation Shielding Information Center, Oak Ridge National Laboratory, Oak Ridge
55. Santa Cruz GA, Zamenhof RG (2004) The microdosimetry of the ^{10}B reaction in boron neutron capture therapy: a new generalized theory. Radiat Res 162:702–710

56. Seppälä T, Auterinen I, Aschan C, Serén T, Bevcizik J, Snellmn M, Huiskamp R, Abo Ramadan U, Kankaanranta L, Joensuu H, Savolainen S (2002) Dose planning with comparison to in-vivo dosimetry for epithermal neutron irradiation of the dog brain. Med Phys 29:2629–2640
57. Stallman FW (1986) LSL-M2: a computer program for least squares logarithmic adjustment of neutron spectra, NUREG/CR-4349, ORNL/TM-9933. Oak Ridge National Laboratory, Oak Ridge
58. Tattam DA, Allen DA, Beynon TD, Constantine G, Green S, Scott MC, Weaver DR (1998) In-phantom neutron fluence measurements in the orthogonal Birmingham boron neutron capture therapy beam. Med Phys 25:1964–1966
59. Toivonen M, Chernov V, Jungner H, Auterinen I, Toivonen A (1999) Response characteristics of LiF:Mg, Cu, P TL detectors in boron neutron capture therapy dosimetry. Radiat Prot Dosimetry 85:373–375
60. Van Vliet-Vroegendeweij C, Wheeler F, Stecher-Rasmussen F, Moss R, Huiskamp R (2001) Microdosimetry model for boron neutron capture therapy: I. Determination of microscopic quantities of heavy particles on a cellular scale. Radiat Res 155:490–497
61. Van Vliet-Vroegendeweij C, Wheeler F, Stecher-Rasmussen F, Huiskamp R (2001) Microdosimetry model for boron neutron capture therapy: II. Theoretical estimation of the effectiveness function and surviving fractions. Radiat Res 155:498–502
62. Verbakel WFAR (2001) Validation of the scanning γ-ray telescope for in-vivo dosimetry and boron measurements during BNCT. Phys Med Biol 46:1–17
63. Wheeler FJ, Parsons DK, Rushton BL, Nigg DW (1990) Epithermal neutron beam design for neutron capture therapy at the PBF and BMRR reactor facilities. Nucl Technol 92:106–118
64. Yamamoto T, Matsumura A, Yamamoto K, Kumada H, Hori N, Torii Y, Shibata Y, Nose T (2003) Characterization of neutron beams for boron neutron capture therapy: in-air radiobiological dosimetry. Radiat Res 160:70–76
65. Zamenhof RG (1997) Microdosimetry for neutron capture therapy: a review. J Neurooncol 33:81–92